Journal of Solid State Chemistry 181 (2008) 1767–1775

Contents lists available at ScienceDirect

Journal of Solid State Chemistry

journal homepage: www.elsevier.com/locate/jssc

Structural and physical properties evolution in the 6H $BaRu_{1-x}Mn_xO_3$ synthesized under high pressure

J.G. Zhao, L.X. Yang, Y. Yu, F.Y. Li, R.C. Yu, C.Q. Jin *

Beijing National Lab for Condensed Matter Physics, Institute of Physics, Chinese Academy of Sciences, Beijing 100080, PR China

ARTICLE INFO

Article history:
Received 8 November 2007
Received in revised form
21 February 2008
Accepted 10 March 2008
Available online 26 March 2008

PACS:
62.50.+p
71.27.+a
72.80.Ga

Keywords:
High-pressure synthesis
6H-perovskite
B-site solid solutions
Weak ferromagnetism
Spin-glass-like magnetism
Electrical conductivity

ABSTRACT

The 6H $BaRu_{1-x}Mn_xO_3$ with the hexagonal $BaTiO_3$ structure was synthesized using high-pressure sintering method. It is found that the lattice parameter deviates from Vegard's law at $x = 0.3$ for the solid solutions due to the charge transfer effects at *B*-site. The substitution of Mn for Ru cations gives rise to the short-range magnetic ordering, due to the disordered arrangement of Ru and Mn cations. The compounds are weak ferromagnetic in the x range 0.05–0.40, with the maximal Curie temperature T_c 175.2 K at $x = 0.10$. They are of spin-glass-like magnetism at lower temperature at $x \geqslant 0.1$. With Mn doping, the 6H $BaRuO_3$ transforms to a semiconductor from the primal metal at $x = 0.30$. The resistance as a function of temperature below about 70 K follows the two-dimensional variable-range hopping conduction mechanism in $BaRu_{0.50}Mn_{0.50}O_3$.

1. Introduction

Recently, the oxide ruthenates have received growing attention for their unique structural and physical properties. For example, in the alkaline-earth ruthenate $ARuO_3$ (A = Ca, Sr, and Ba), $BaRuO_3$ rather crystallizes into the hexagonal perovskite structure at ambient or lower synthesis pressure [1,2], than the orthorhombic perovskite structure like $SrRuO_3$ and $CaRuO_3$ [3,4]. Three types of hexagonal perovskite $BaRuO_3$, namely 9R, 4H, and 6H, have been reported, where the number is the amount of BaO_3 layers in a unit cell, and the R and H denote the rhombohedral and hexagonal structures, respectively. At about 110 K, the 9R $BaRuO_3$ becomes insulator-like from metallic behavior due to the pseudogap open [5,6]. It is of short-range antiferromagnetic ordering below the Néel point of about 440 K, due to the antiferromagnetic arrangement between the adjacent electronic spin in the Ru_3O_{12} trioctahedrons [6,7]. The 4H $BaRuO_3$ is a normal paramagnetic Fermi-liquid metal down to liquid helium temperature [5]. The 6H $BaRuO_3$ is an abnormal paramagnetic metal deviated from the Fermi-liquid behavior at low temperature [8]. There is a strong electron–electron correlation in the 4H and 6H forms.

The chemical substitution of M cation for 1/3 Ru cation at ambient pressure can make the 9R $BaRuO_3$ transform to the $Ba_3MRu_2O_9$ compounds, where M = alkali metals, alkaline-earth elements, 3*d* transition metals, and lanthanide elements. They adopt the normal or distorted hexagonal $BaTiO_3$ structure [9], as summarized by Quarez et al. [10]. For most $Ba_3MRu_2O_9$ compounds, the arrangement of M and Ru cations is ordered: M cation and Ru cation occupy the corner-sharing octahedral sites (in the MO_6 octahedron) and the face-sharing octahedral sites (in the Ru_2O_9 dioctahedron), respectively. The chemical substitution results in the change of physical properties. All these compounds with Ru-site substitution are semiconducting, although there is the unpaired d or f electron in most M cations, e.g. Fe^{3+}, Pr^{4+} [11–13]. Their magnetic properties are very complex, containing the contributions of M cations and Ru–Ru direct interaction.

The $BaRu_{1-x}Mn_xO_3$ solid solutions are the special materials in the Ru-site substitution compounds. They keep the primal 9R form of $BaRuO_3$ in a large substituting range, with the disordered arrangement of Ru and Mn cations [14,15]. $BaMnO_3$ adopts the 2H form, which contains chains of face-sharing octahedrons parallel to *c*-axis [16,17]. Under high pressure and high temperature, the 2H $BaMnO_3$ can transform to the 9R and 4H forms [18], which is similar with that in $BaRuO_3$ [2]. So $BaRu_{1-x}Mn_xO_3$ will transform to the other hexagonal perovskite structures from the initial 9R or 2H forms under sufficient high synthesis pressure. Fig. 1 shows

* Corresponding author.
E-mail address: Jin@aphy.iphy.ac.cn (C.Q. Jin).

0022-4596/$ - see front matter © 2008 Elsevier Inc. All rights reserved.
doi:10.1016/j.jssc.2008.03.014

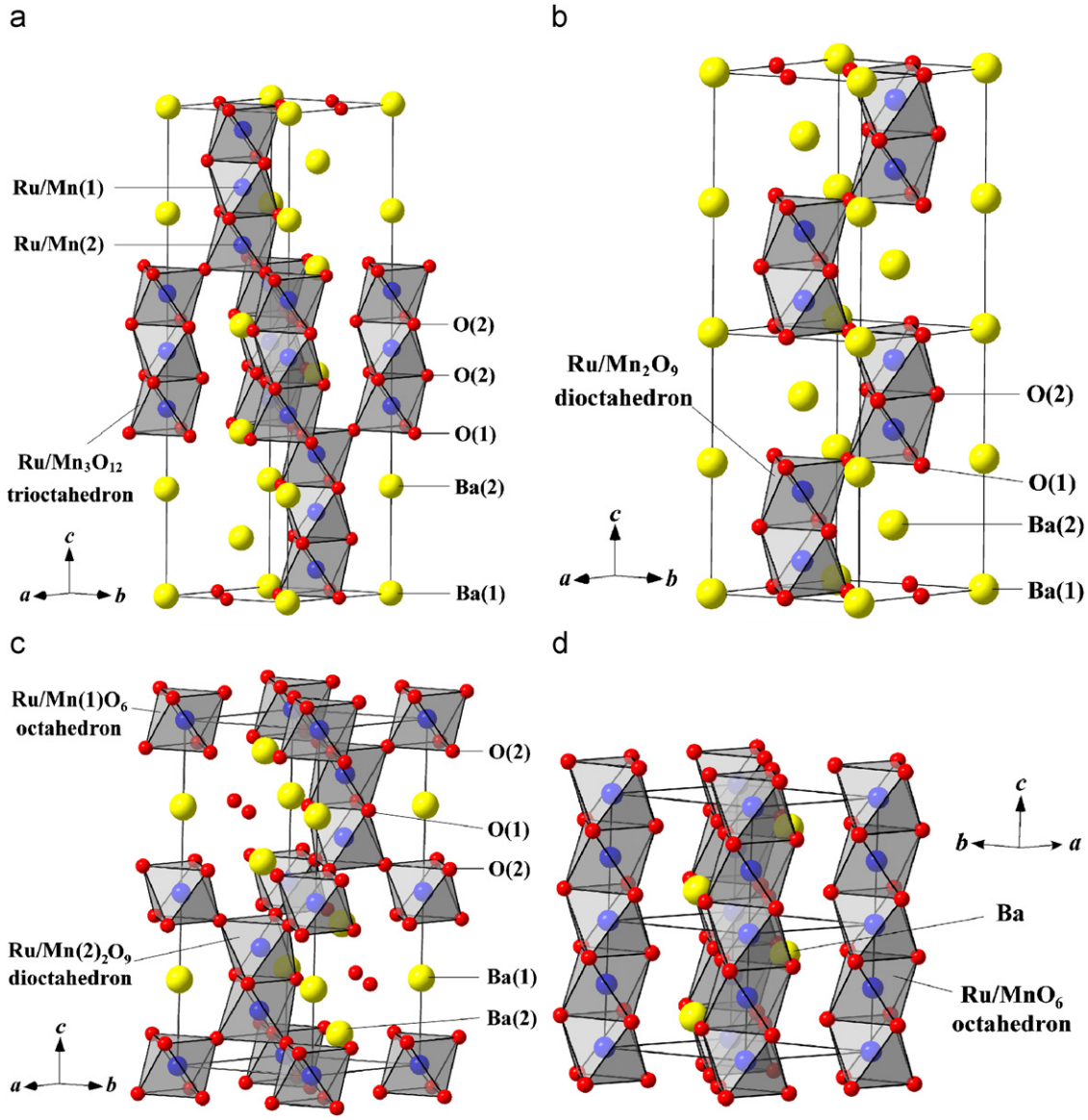

Fig. 1. The schematic views of the four crystallographic forms of $BaRu_{1-x}Mn_xO_3$: (a) 9R form, (b) 4H form, (c) 6H form, and (d) 2H form. The MO_6 octahedrons are represented by geometrical coordination (*M* at the center, O at corners). The unit cells are outlined.

the schematic views of the 9R, 4H, 6H, and 2H forms of $BaRu_{1-x}Mn_xO_3$.

Although the properties of end-number compounds of $BaRu_{1-x}Mn_xO_3$ are investigated, those of the intermediate ones are not well studied, especially for the 6H phases. In fact, the solid solutions of Mn and Ru exist widely in the perovskite-type compounds, e.g. $CaRu_{1-x}Mn_xO_3$ [19], $SrRu_{1-x}Mn_xO_3$ [20]. Since the 3*d* electron orbitals of the Mn cations are more localized than those of the 4*d* or 5*d* elements, the substitution of Mn for Ru cation obviously affects the electrical and magnetic properties of the parent compounds. For example, the substitution of Mn in $CaRuO_3$ gives rise to the Kondo-like effect, with the Kondo temperature T_K about 48 K, while *x* is in the range 0.02–0.3 [19]. In $SrRuO_3$, Mn doping at the Ru-site drives the compound from the itinerant ferromagnetism through a quantum critical point at $x_c = 0.39$ to the insulating antiferromagnetism [20].

In this paper, we report the high-pressure synthesis of the 6H $BaRu_{1-x}Mn_xO_3$. The structural, magnetic and electrical properties were characterized. It is found that the 6H $BaRu_{1-x}Mn_xO_3$ ($0.05 \leqslant x \leqslant 0.40$) are weak ferromagnetic with short-range magnetic ordering. The results were also compared to the respective 9R and 4H forms in the context of the octahedron arrangements.

2. Experimental

2.1. Synthesis

The ambient phases of $BaRu_{1-x}Mn_xO_3$ were synthesized by using the method of conventional solid-state chemical reaction. The starting materials were barium carbonate (99.9% purity), ruthenium metal (99.9% purity), and Mn_2O_3 (99.9% purity). Stoichiometric quantities of materials were mixed together, ground about 30 min in an agate mortar, and placed into an Al_2O_3 crucible. Then the powder was calcined for about 12 h at 900 °C in air. The calcined powder was reground, pressed into a pellet at the pressure of 10 MPa, and sintered at 1000 °C for about 72 h in air with twice intermediate regrinding. The products adopted the 9R structure in the range 0.0–0.80 and crystallized into the 2H structure at $0.8 < x \leqslant 1.0$.

A conventional cubic-anvil type high-pressure facility was used to perform the high-pressure and high-temperature experiments. The ambient $BaRu_{1-x}Mn_xO_3$ were pressed into pellets of 5.0 mm diameter, and then wrapped with gold foil to avoid contamination. The pellets were put into an h-BN sleeve which was in turn inserted into a graphite tube heater. Pyrophyllite was used as the pressure-transmitting medium. The treating process was carried out at 1.5–5.0 GPa and 1000 °C for about 30 min, followed by a quench from high temperature before releasing pressure with the rate about 0.6 GPa/min. The 6H $BaRu_{1-x}Mn_xO_3$ are obtained at 5.0 GPa in the range 0.0–0.50.

2.2. X-ray diffraction analysis

The structures of our samples were checked by the powder X-ray diffraction (XRD) with Cu$K\alpha$ radiation at room temperature, using a Rigaku diffractometer (MXP-AHP18). The experimental data of the 6H forms were collected in 2θ-steps of 0.02° and 3 s counting time in the range 10–120° and analyzed with Rietveld method by using the FullProf program [21].

2.3. Magnetic susceptibility measurements

The relationships of magnetic susceptibility versus temperature were obtained using a SQUID magnetometer (Quantum Design, MPMS-5S) in the temperature range 5–300 K. Data were collected under both zero-field-cooled (ZFC) and field-cooled (FC) conditions. The samples were cooled under zero magnetic field, and the magnetization was measured upon heating and then upon cooling under a 0.1 T applied field. For the 6H forms, the magnetic field dependences of magnetization were measured at 5 K.

2.4. Electrical resistivity measurements

The measurements of temperature dependences of electrical resistivity were performed by using the standard four-probe method with Ag paste contacts.

3. Results and discussion

3.1. Crystal structure

Fig. 2(a)–(d) show the observed and fitted XRD patterns of the 6H $BaRu_{1-x}Mn_xO_3$ at $x = 0.0$, 0.1, 0.3, and 0.5, and the insets show the details in the range 80–120°. There are two possible ordered arrangements of Mn and Ru cations in the 6H $Ba_3MnRu_2O_9$, as shown in Fig. 3(a) and (b). In the ordering-I structure, one Ru cation occupies the corner-sharing octahedral site, and the other Ru cation and Mn cation occupy the face-sharing octahedral sites. In the ordering-II structure, Mn and Ru cations occupy the corner-sharing octahedral site and face-sharing octahedral sites, respectively. We fitted their XRD patterns, as shown in Fig. 3(c), together with those of the disordered structure and the experimental data for $x = 0.3$ sample in which x is close to 1/3. The experimental XRD pattern is very similar with the fitted one of disordered structure, but it is different from those of the ordered structures, especially for the peak (002), (100), and (112). So the arrangement of Mn and Ru cations is disordered with Mn substituted randomly for Ru cations, due to the comparable radius of Mn and Ru cations [22] and close electrovalence. And we use M to denote the B-site cations.

The XRD data are fitted with the $P6_3/mmc$ space group and analyzed with the Rietveld method. Table 1 lists the lattice parameters, atom positional parameters, and R-factors. The obtained R_p, R_{wp}, and R_{exp} factors indicate the good consistence of the refined results. Table 2 lists the main interatomic distances and bond angles. The average $M(2)$–O distance is decreasing with increasing x except the value of $BaRu_{0.90}Mn_{0.01}O_3$. The $M(2)$–$M(2)$ distance for the two metal cations connected directly in the M_2O_9 dioctahedron is increasing with x and then keeps the value of about 2.61 Å from $x = 0.2$. The O(2)–$M(1)$–O(2) angles are nearly equal to 90° or 180°, which indicates that the $M(1)O_6$ octahedrons are almost ideal without bond bending. The O(1)–$M(2)$–O(1), O(2)–$M(2)$–O(2), and O(1)–$M(2)$–O(2) angles deviate from 90° or 180°, indicating that the distortion of the $M(2)_2O_9$ dioctahedrons is larger than that of the $M(1)O_6$ octahedrons for all the solid solutions.

Fig. 2(e) shows the relationship of the volume of one chemical formula unit ($V/6$) versus the Mn content x in the 6H $BaRu_{1-x}Mn_xO_3$. The inset shows the x dependence of normalized lattice parameters. The values of a- and c-axis are both decreasing with increasing x, and the change of c with x is larger than that of a. The relationship of $V/6$ versus x should be linear because of the disordered arrangement of Ru and Mn cations. However, there is an obvious variation while x is equal to 0.30. The value of $\partial(V/6)/\partial x$ is $-1.77(7)$ Å^3 for $x \leqslant 0.30$ and $-2.86(3)$ Å^3 for $x \geqslant 0.30$. So the x dependence of $V/6$ deviates from the Vegard's law. The charge transfer from [Ru^{5+}(0.565 Å)+Mn^{3+}(0.645 Å)] to [Ru^{4+}(0.62 Å)+Mn^{4+}(0.53 Å)] exists in our $BaRu_{1-x}Mn_xO_3$ samples, where the value in parenthesis is the radius of cation in the octahedral crystal field in Shannon table [22]. This charger transfer is a common phenomenon in the Mn and Ru solid solutions [23–26]. The similar kink in the relationship of cell volume versus x was also found in $SrRu_{1-x}Cr_xO_3$ [27], which is also due to the charger transfer from (Ru^{5+}+Cr^{3+}) to (Ru^{4+}+Cr^{4+}). We thought that the Mn and Ru charger transfer is the main reason of discontinuity in the V–x relationship. While x is less than 0.30, Mn^{3+} is the main ionic state of Mn cations, so Ru^{4+} and Ru^{5+} coexist in the samples. The average radius of Ru^{5+} and Mn^{3+} cations is equal to 0.605 Å, which is smaller than that of Ru^{4+} cation, so the volume of unit cell is decreasing with the doping of Mn. While x is larger than 0.30, Mn^{4+} cations come into being, so the Mn^{4+} and Mn^{3+} cations coexist in the compounds, which induces the accelerated shrinkage of volume with increasing x, because the average ion radius of Mn^{4+} and Ru^{4+} (0.575 Å) is smaller than that of Mn^{3+} and Ru^{5+} (0.605 Å). This charger transfer results in the change of magnetic and electrical properties with increasing x, as mentioned in the following sections.

3.2. Magnetic properties

Fig. 4(a) shows temperature dependences of magnetic susceptibility in the range 5–300 K of the 6H $BaRu_{1-x}Mn_xO_3$. Only the ZFC curve is shown for the correlation enhanced paramagnetic 6H $BaRuO_3$ [8], because there is no obvious deviation between ZFC and FC mode. For the even slightly Mn-doped ($\geqslant$5%) compounds, a clear difference between ZFC and FC curves was observed nearby the magnetic ordering temperature. The pure 6H $BaRuO_3$ is paramagnetic, without the magnetic ordering in the experimental temperature range. Substitution of Mn for Ru cations in $BaRuO_3$ gives rise to the magnetic ordering. However, the disordered arrangement of Ru and Mn cations results in the short-range magnetic interaction without long-range ordering. At $0 < x \leqslant 0.40$, the 6H $BaRu_{1-x}Mn_xO_3$ are weak ferromagnetic with the maximal Curie temperature T_c of 175.2 K at $x = 0.10$, and behave spin-glass-like state at lower temperature, for the separation between ZFC and FC curves. The spin-glass-like behavior at low temperature exists in many Ru and Mn solid solutions, such as $CaMn_{1-x}Ru_xO_3$ [28], the 9R $Ba_3MnRu_2O_9$ [29], $LaMn_{0.65}Ru_{0.3}O_3$

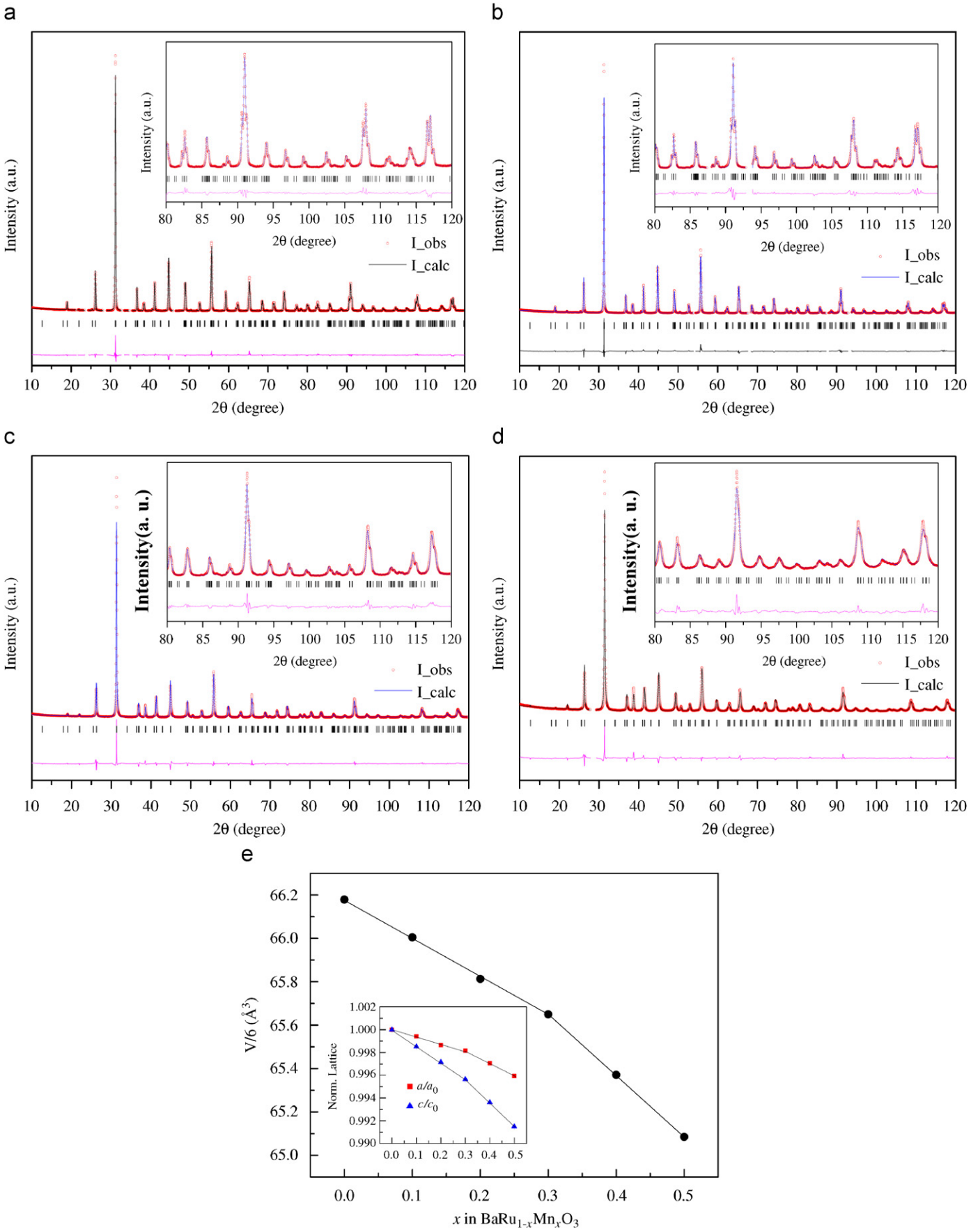

Fig. 2. (a)–(d) The experimental (open circle) and fitted (solid line) X-ray diffraction patterns for the 6H $BaRu_{1-x}Mn_xO_3$ at $x = 0.0, 0.1, 0.3, 0.5$. The difference plots between observed and calculated patterns are shown at the bottom. The positions of the Bragg reflections are shown by the vertical lines. The insets show the details of patterns in the range 80–120°. (e) The relationship of the volume of one chemical formula unit ($V/6$) versus x. The inset shows the relationships of normalized lattice parameters versus x.

[30], $LaMn_xRu_{1-x}O_3$ [31], $A_{0.5}La_{0.5}Mn_{0.5}Ru_{0.5}O_3$ (A = Ca, Sr, Ba) [32], $La_{0.6}Pb_{0.4}Mn_{0.5}Ru_{0.5}O_3$ [33], and so on. There should be a frustration in the 6H $BaRu_{1-x}Mn_xO_3$, because the disordered arrangement of Mn and Ru cations results in the presence of competing interactions that induce the spin-glass-like behavior. While x is equal to 0.50, the magnetic property becomes spin-glass-like magnetism completely, with the glass transition temperature T_g about 50 K. The relationships of T_c and T_g versus x are shown in the inset of Fig. 4(a). T_g is increasing with x. While x is equal to 0.50, T_g is almost equal to that of $BaRu_{0.60}Mn_{0.40}O_3$.

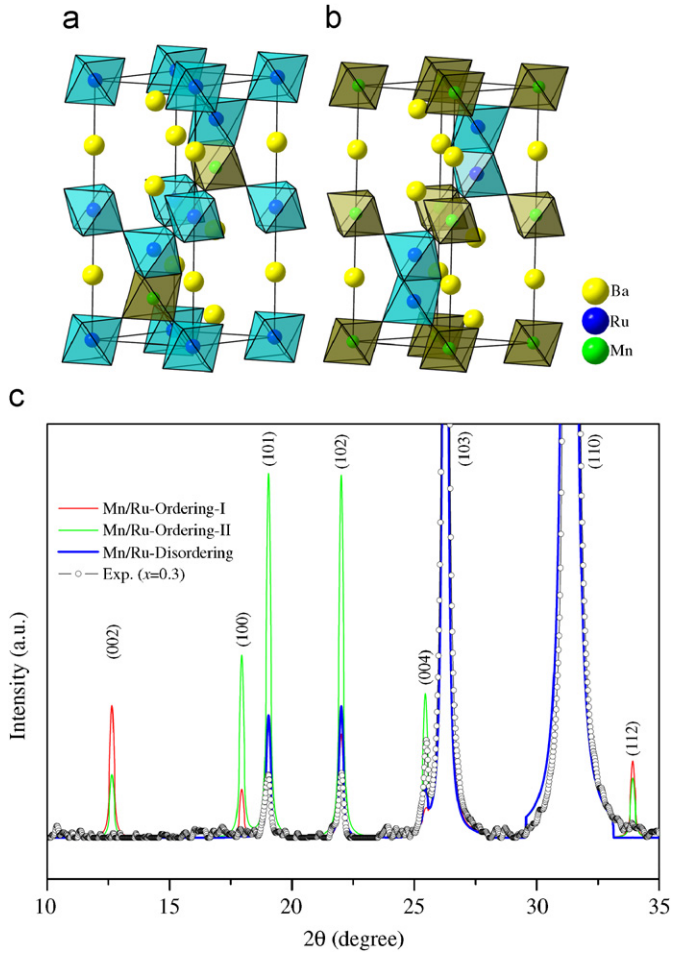

Fig. 3. The schematic views of two possible ordered arrangements of Mn and Ru cations in the 6H $Ba_3MnRu_2O_9$: (a) ordering-I, and (b) ordering-II. (c) Fitting XRD patterns from (a) and (b), together with those of the disordered structure and the experimental data for $x = 0.3$ sample.

The paramagnetic susceptibility χ above T_c of the 6H $BaRu_{1-x}Mn_xO_3$ can be fitted to the following equation [34]:

$$\chi = \chi_{CW}(T) + \chi_{EP}(T) = \frac{C}{T-\theta} + \chi_0(1 - AT^2), \quad (1)$$

where χ_{CW} and χ_{EP} are the Curie–Weiss (CW) and exchange-enhanced Pauli (EP) contributions to magnetic susceptibility, respectively. The fitted results about the magnetic properties are summarized in Table 3. The paramagnetic effective magnetic moment μ_{eff} is obtained from the Curie constant C with the formula $\mu_{eff} = 2.828\sqrt{C}$. For the 6H $BaRu_{1-x}Mn_xO_3$, μ_{eff} is smaller than the theoretic value calculated in the spin only model for the Mn and Ru cations, due to spin–orbital coupling effect and the suppressing on moments of metal cations by strong metal–metal bonding. With increasing x, μ_{eff} is increasing except the value of $BaRu_{0.95}Mn_{0.05}O_3$. The increase of μ_{eff} is mainly due to the enhancement of valence of cations and the superexchange interaction between Mn and Ru cations. The paramagnetic Curie temperature θ is positive in the range 0.05–0.50, which indicates that the interaction between electronic spins in the two adjacent B-sites is ferromagnetic, being different from that in the undoped 6H $BaRuO_3$ [8].

Fig. 4(b) shows the M–H curves at 5 K while x is in the range 0.0–0.50. The inset shows the enlargement between −0.5 and 0.5 T. For the samples with substitution of Mn, the M–H curves are weak hysteresis loops, without any saturated trend in the experimental magnetic field range. The magnetic moments of all the samples at the maximal magnetic field are much smaller than the theoretic values of Mn or Ru cations, which is consistent with the short-range magnetic ordering.

Mn cations substitution results in the change of magnetic property for the 6H $BaRuO_3$. The weak ferromagnetism of the 6H $BaRu_{1-x}Mn_xO_3$ is attributed to the interaction between Mn and Ru cations. According to the theory in Ref. [35], the 180° cation–anion–cation superexchange interaction between Mn^{3+} (high-spin electronic state: $t_{2g}^3e_g^1$) and other cations, i.e. Ru^{4+} (t_{2g}^4), Ru^{5+} (t_{2g}^3),

Table 1
Structural parameters for the 6H $BaRu_{1-x}Mn_xO_3$ ($0 \leqslant x \leqslant 0.50$)

	x in $BaRu_{1-x}Mn_xO_3$					
	0.00	0.10	0.20	0.30	0.40	0.50
a (Å)	5.7127(1)	5.7096(1)	5.7049(1)	5.7026(2)	5.6961(1)	5.6895(2)
c (Å)	14.0499(2)	14.0301(2)	14.0099(3)	13.9886(5)	13.9605(5)	13.9309(7)
Ba(1) B (Å^2)	0.35(3)	0.38(4)	0.12(5)	0.42(5)	0.57(4)	0.44(4)
Ba(2) z	0.08960(6)	0.09001(8)	0.0897(1)	0.0893(1)	0.0895(1)	0.0894(1)
Ba(2) B (Å^2)	0.22(2)	0.12(3)	0.10(4)	0.14(3)	0.49(3)	0.43(4)
M(1) B (Å^2)	0.62(4)	0.63(7)	1.17(8)	0.31(8)	0.60(8)	0.37(9)
M(2) z	0.65869(6)	0.65849(9)	0.6568(1)	0.6567(1)	0.6566(1)	0.6564(2)
M(2) B (Å^2)	0.40(3)	0.14(5)	0.30(7)	0.90(8)	0.75(8)	0.58(9)
O(1) x	0.517(1)	0.509 (1)	0.516(1)	0.516(1)	0.514(1)	0.516(1)
O(1) B (Å^2)	1.7(2)	1.1(2)	0.9(2)	1.4(2)	1.0(2)	0.9(2)
O(2) x	0.836(1)	0.836(1)	0.836(1)	0.830(1)	0.830(1)	0.829(1)
O(2) z	0.078(1)	0.081(1)	0.081(1)	0.079(1)	0.080(1)	0.079(1)
O(2) B (Å^2)	0.4(1)	0.9(1)	1.2(1)	1.0(2)	1.4(1)	1.2(1)
R_p (%)	6.12	7.05	9.65	9.15	7.93	8.63
R_{wp} (%)	8.47	9.59	14.2	11.9	10.5	11.4
R_{exp} (%)	7.54	6.50	6.86	6.48	7.41	9.72
χ^2	1.26	2.17	4.30	3.37	2.03	2.54

Table 2
Selected interatomic distances (Å) and angles (deg) for the 6H $BaRu_{1-x}Mn_xO_3$ ($0 \leqslant x \leqslant 0.50$)

	x in $BaRu_{1-x}Mn_xO_3$					
	0.00	0.10	0.20	0.30	0.40	0.50
Ba(1)–O(1) × 6	2.861(4)	2.856(4)	2.857(4)	2.856(4)	2.851(4)	2.849(4)
Ba(1)–O(2) × 6	2.911(13)	2.876(13)	2.869(13)	2.923(13)	2.906(13)	2.918(13)
Ba(2)–O(1) × 3	2.895(4)	2.838(6)	2.881(6)	2.882(6)	2.863(6)	2.984(6)
Ba(2)–O(2) × 6	2.861(4)	2.855(4)	2.855(4)	2.855(4)	2.851(4)	2.845(4)
Ba(2)–O(2) × 3	2.890(13)	2.923(13)	2.919(13)	2.854(13)	2.863(13)	2.723(13)
M(2)–O(1) × 3	1.959(5)	2.020(6)	1.980(5)	1.979(5)	1.992(5)	1.976(6)
M(2)–O(2) × 3	2.023(11)	1.992(11)	1.982(11)	1.945(11)	1.934(11)	1.929(11)
M(2)–O (average)	1.991(8)	2.006(9)	1.981(8)	1.962(8)	1.963(8)	1.953(9)
M(2)–*M*(2)	2.566(1)	2.568(2)	2.611(2)	2.610(2)	2.608(2)	2.608(4)
M(1)–*M*(2)	3.9811(6)	3.9763(7)	3.9591(8)	3.9554(8)	3.9490(8)	3.942(1)
M(1)–O(2) × 6	1.958(10)	1.984(10)	1.978(10)	2.01 (1)	2.015(10)	2.013(10)
O(1)–*M*(2)–O(1) × 3	81.8(1)	83.9(1)	81.3(1)	81.3(1)	81.8(1)	81.2(1)
O(1)–*M*(2)–O(2) × 6	93.1(3)	91.4(3)	92.1(3)	93.3(3)	92.4(3)	93.3(2)
O(2)–*M*(2)–O(2) × 3	91.7(3)	93.1(3)	94.0(3)	91.8(3)	92.7(3)	91.8(3)
O(1)–*M*(2)–O(2) × 3	173.2(3)	173.6(3)	171.2(3)	172.7(3)	172.7(3)	172.7(3)
M(2)–O(1)–*M*(2)	81.8(1)	78.9(1)	82.5(1)	82.5(1)	81.8(1)	82.6(1)
O(2)–*M*(1)–O(2) × 6	88.3(3)	89.7(3)	89.6(3)	87.3(3)	87.8(3)	87.1(3)
O(2)–*M*(1)–O(2) × 6	91.7(3)	90.5(3)	90.4(3)	92.7(3)	92.3(3)	92.9(3)
O(2)–*M*(1)–O(2) × 3	180.0(5)	179.8(4)	180.0(5)	180.0(4)	180.0(3)	180.0(4)
M(2)–O(2)–*M*(1)	180.0(6)	178.1(6)	177.4(6)	179.4(6)	179.9(6)	179.2(6)

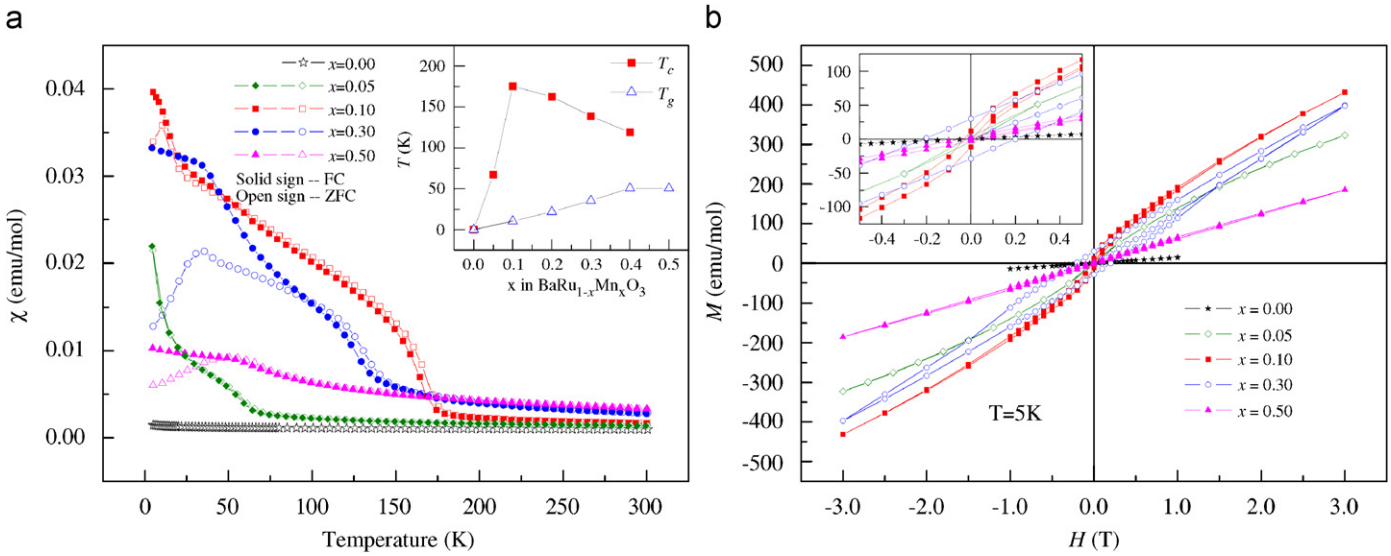

Fig. 4. (a) Temperature dependences of magnetic susceptibility of the 6H $BaRu_{1-x}Mn_xO_3$. The inset shows the relationships of Curie temperature T_c and spin glass temperature T_g versus x. (b) The hysteresis loops at 5 K. The inset shows the enlargement at $|H| \leqslant 0.5$ T.

Table 3
Fitted results of χ–T curves for the 6H $BaRu_{1-x}Mn_xO_3$ ($0 \leqslant x \leqslant 0.50$) in the form of Eq. (1)

	x in $BaRu_{1-x}Mn_xO_3$						
	0.00	0.05	0.10	0.20	0.30	0.40	0.50
θ (K)	−17.5(5)	40(1)	167.31(7)	144(1)	119(1)	57(1)	8(1)
C (emu K/mol)	0.0084(2)	0.044(3)	0.0136(4)	0.033(3)	0.081(7)	0.33(1)	0.333(8)
μ_{eff} (μ_B)	0.259(3)	0.59(2)	0.330(5)	0.51(2)	0.80(3)	1.63(2)	1.63(2)
χ_0 (10^{-3} emu/mol)	1.056(2)	1.56(3)	2.14(2)	2.99(5)	3.7(1)	2.51(8)	2.83(5)
A (10^{-6} K^{-2})	1.35(2)	2.7(1)	3.00(9)	3.67(9)	4.3(2)	3.42(9)	2.95(7)

and Mn^{4+} (t_{2g}^3), is ferromagnetic and antiferromagnetic for the quasistatic and static Jahn–Teller distortions, respectively. In our samples, the Jahn–Teller distortion is quasistatic, due to the alterable valence of Mn and Ru cations, which results in that the superexchange interaction is ferromagnetic. In the M_2O_9 dioctahedron, the direct interaction between the two neighboring

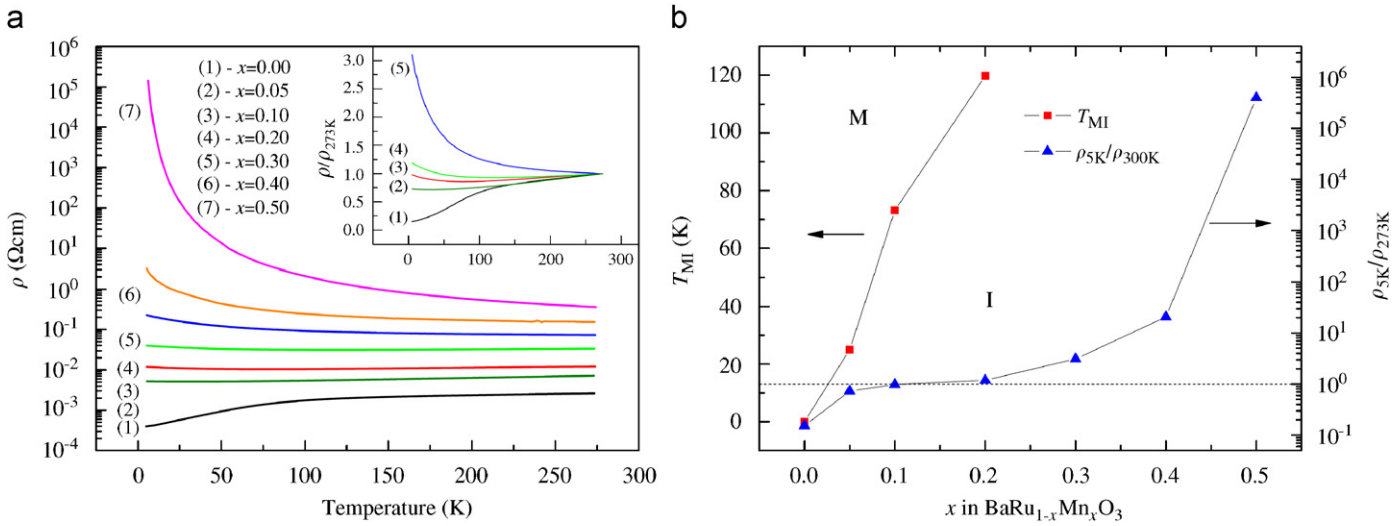

Fig. 5. (a) Temperature dependences of electrical resistivity of the 6H $BaRu_{1-x}Mn_xO_3$. The inset shows the normalized resistivity to the values at 273 K in the range 0.0–0.30. (b) The relationships of metal–insulator transition temperature T_{MI} and the ratio $\rho_{5\,K}/\rho_{273\,K}$ versus x. The sign "M" and "I" denote the metallic and insulator-like regions, respectively.

cations is stronger than the 90° *cation–anion–cation* interaction for the short *M–M* distances. In the 6H $BaRu_{1-x}Mn_xO_3$, the portion of corner-shared MO_6 octahedron is higher than that of face-shared one. So the contribution for magnetism of *M*–O–*M* interaction between two MO_6 octahedrons is more important than that in the M_2O_9 dioctahedron. The change of magnetism is closely related to the charge transfer mentioned in Section 3.1. While x is less than 0.3, Mn^{3+}, Ru^{4+} and Ru^{5+} cations coexist in the samples. The superexchange interaction between Mn^{3+} and other cations is ferromagnetic, which gives rise to the ferromagnetic ordering in our samples. While x is larger than 0.30, Mn^{4+}, Ru^{4+} and Ru^{5+} cations are the main ionic state in the 6H $BaRu_{1-x}Mn_xO_3$. The interaction between Ru^{4+}, Ru^{5+}, and Mn^{4+} cations is weak antiferromagnetic [35]. So the samples lose gradually the weak ferromagnetism. At $x = 0.50$, Mn^{4+} is the main ionic state of Mn cations, the sample behaves only spin-glass-like magnetism at low temperature.

3.3. Electrical properties

The temperature dependences of electrical resistivity in the range 5–273 K of the 6H $BaRu_{1-x}Mn_xO_3$ are shown in Fig. 5(a). The inset shows the normalized electrical resistivity while x is in the range 0.0–0.30. The resistivity change is mainly due to the scattering at Mn with the localized electrons. There is no obvious anomaly in the ρ–T curves at T_c, which is consistent with the short-range magnetic ordering. The 6H $BaRuO_3$ maintains the metallic behavior down to the lowest temperature in our experiments [8]. In the range 0.05–0.20, the samples are metallic at high temperature and become insulator-like at lower temperature. The relationship of metal–insulator transition temperature T_{MI} versus x is shown in Fig. 5(b). T_{MI} is increasing with increasing x. The transition from metal to semiconductor at low temperature is attributed to the localization of 3*d* electrons of Mn cations, since the localized and itinerant electrons coexist in our samples. While x is equal to 0.30, the sample is semiconducting in the experimental temperature range and T_{MI} may be above room temperature. Fig. 5(b) shows the relationship of $\rho_{5\,K}/\rho_{273\,K}$ versus x. According to the similar judgment in Ref. [36], the ratio of resistivity at 5 K to that at 273 K can reflect the electrical property of compounds: $\rho_{5\,K}/\rho_{273\,K} < 1$ is corresponding to a metal, and $\rho_{5\,K}/\rho_{273\,K} > 1$ is corresponding to a semiconductor. The sample $BaRu_{0.90}Mn_{0.10}O_3$ and $BaRu_{0.80}Mn_{0.20}O_3$ can be approximately viewed as metals, since their $\rho_{5\,K}/\rho_{273\,K}$ are close to 1. The semiconducting property of samples is increasing with increasing x. The electrical resistivity of $BaRu_{0.70}Mn_{0.30}O_3$ and $BaRu_{0.60}Mn_{0.40}O_3$ is much smaller than that of $BaRu_{0.50}Mn_{0.50}O_3$ at 5 K, which indicates that the localized electrons of Mn cations are the main parts in the latter. The temperature dependences of electrical resistivity of $BaRu_{0.70}Mn_{0.30}O_3$ and $BaRu_{0.60}Mn_{0.40}O_3$ do not obey activation law or other power law. While x is equal to 0.50, the sample is a normal semiconductor, with the electrical resistivity of about $10^5\,\Omega$ cm at 5 K. The temperature dependence of electrical resistivity follows the law $\rho = \rho_0 \exp[(T_M/T)^{1/3}]$ below about 70 K, which indicates that the electrical transport behavior obeys the two-dimensional variable-range hopping (VRH) conduction mechanism, rather than the activation law, like that in the perovskite-type $SrRu_{0.41}Mn_{0.59}O_3$ [20]. According to fitting the data, the parameter T_M of $3.783(7) \times 10^4$ K and ρ_0 of $4.35(3) \times 10^{-4}$ Ω cm are obtained.

The influence of charge transfer to transport property is not obvious while x is less than 0.4. The electrical resistivity is gradually increasing with increasing x. At $x = 0.5$, the electrical resistivity and $\rho_{5\,K}/\rho_{273\,K}$ are drastically increasing, comparing with those of the $x = 0.4$ sample. There is scarcely Mn^{3+} cations in the 6H $BaRu_{0.50}Mn_{0.50}O_3$, which induces no interaction between the adjacent cations through e_g electrons. So the sample behaves obviously semiconducting, with large electrical resistivity and 2D VRH conduction mechanism below about 70 K.

3.4. Comparison with the 9R and 4H forms

In order to study the effect of structure on the physical properties for $BaRu_{1-x}Mn_xO_3$, we compare the magnetic and electrical properties of the 9R, 4H and 6H forms. Fig. 6(a) shows the temperature dependences of electrical resistivity of the 9R, 4H and 6H $BaRu_{0.90}Mn_{0.10}O_3$, and Fig. 6(b) shows their χ–T curves. The 9R form is a semiconductor in the experimental temperature range. Both the 4H and 6H forms are metallic at high temperature and become insulator-like at lower temperature, and their T_{MI} are 61.7 and 73.2 K, respectively. In the dioctahedron of the 4H and 6H forms, there is only interaction between two neighboring *M* cations, forming *M–M* dimer. But, in the trioctahedron of the 9R form, the interaction between two outer *M* cations gives rise to

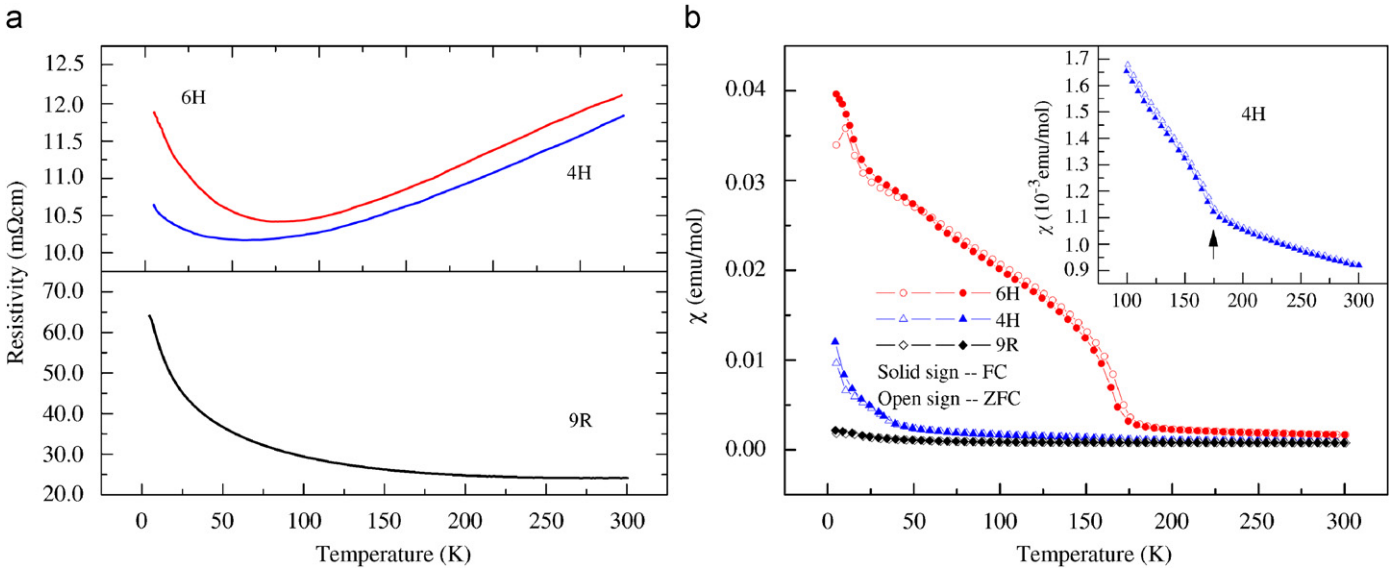

Fig. 6. (a) The comparison of the ρ–T curves for the 9R, 4H, and 6H $BaRu_{0.90}Mn_{0.10}O_3$. (b) The comparison of the χ–T curves for the three forms. The inset shows the details of the 4H form in the range 100–300 K.

M–M–M trimer, resulting in the different electronic state. The strong interaction between the adjacent M cations results in the electron localization, which is stronger than that in the 4H and 6H forms. The 9R form is paramagnetic in the experimental temperature range. Comparing with the undoped sample [5,8], the Mn doping results in the superexchange interaction between Mn and Ru cations, which makes the 9R $BaRu_{0.9}Mn_{0.1}O_3$ become a paramagnet. Although the relationships of electrical resistivity versus temperature of the 6H and 4H forms are similar, the difference between their χ–T curves is very obvious. The 6H form is weak ferromagnetic, with the T_c 175.2 K, and spin-glass-like below about 10 K. The 4H form is paramagnetic, and there is an obvious turning point at about 175 K, as indicated with an arrowhead in the inset of Fig. 6(b). The different crystal structures result in the different magnetic properties. Unlike the quasi one-dimensional chain type structure for the 9R form composed of M_3O_{12} trioctahedron and 4H form composed of M_2O_9 dioctahedron, the arrangement of M cations in the 6H form is more close to three-dimension in that it has a single corner-sharing MO_6 octahedron between two M_2O_9 dioctahedrons, indicating the higher portion of corner-sharing MO_6 octahedron than those of the former two phases. The paramagnetic susceptibility of the three forms can be fitted with Eq. (1), and the fitted results are summarized in Table 4. The negative sign of paramagnetic Curie temperature θ of the 9R form indicates the interaction between two adjacent electronic spins is antiferromagnetic, in contrast with that in the 4H and 6H forms.

Due to the disordered arrangement of Mn and Ru cations, we consider the average interaction between two adjacent M cations in $BaRu_{1-x}Mn_xO_3$. The superexchange interaction between electronic spins in the two metal cations through O anions in the corner is ferromagnetic, rather than antiferromagnetic. However, the direct interaction between electronic spins in the two metal cations in the polyhedrons is antiferromagnetic. The magnetic property of $BaRu_{1-x}Mn_xO_3$ is the competition of the two magnetic interactions. In the undoped samples, the 180° Ru–O–Ru superexchange interaction is weak, but the Ru–Ru direct interaction is strong, so $BaRuO_3$ is short-range antiferromagnetic or paramagnetic [5,8]. Mn doping enhances the superexchange interaction, mediated by the O ions, but weakens the M–M direct interaction, due to the localized electrons in the Mn cations. In the 6H form, the superexchange interaction between $M(1)$ and $M(2)$ cations is more important, due to the single MO_6 octahedron in the crystal structure. So the 6H form behaves weak ferromagnetism.

Table 4
Fitted results of χ–T curves for the 9R, 4H, and 6H $BaRu_{0.90}Mn_{0.10}O_3$ in the form of Eq. (1)

	9R	4H	6H
θ (K)	−2.4(3)	121(8)	167.31(7)
C (emu K/mol)	0.0184(3)	0.010(2)	0.0136(4)
μ_{eff} (μ_B)	0.384(3)	0.28(3)	0.330(5)
χ_0 (10^{-3} emu/mol)	0.698(3)	1.00(3)	2.14(2)
A (10^{-6} K^{-2})	−0.34(6)	1.5(1)	3.00(9)

4. Conclusions

In summary, the 6H $BaRu_{1-x}Mn_xO_3$ was synthesized by using the high-pressure technique, and the XRD pattern, electrical resistivity, and magnetic susceptibility were obtained. Structural data indicated that they crystallize into the hexagonal $BaTiO_3$ structure, with the disordered arrangement of Ru and Mn cations. The deviation of lattice parameter from Vegard's law at $x = 0.3$ indicates the charge transfer effects at B-site. The localized and itinerant electrons coexist in Mn-substituted $BaRuO_3$. The measurements of electrical and magnetic properties showed that the substitution of Mn for Ru cation results in short-range ferromagnetic ordering and semiconducting properties in the 6H $BaRu_{1-x}Mn_xO_3$.

Acknowledgments

This work was supported by nsf & MOST of China through the research projects (2005CB724402;2007CB925003;10674160).

References

[1] P.C. Donohue, L. Katz, R. Ward, Inorg. Chem. 4 (1964) 306–310.
[2] J.M. Longo, J.A. Kafalas, Mater. Res. Bull. 3 (1968) 687–692.

[3] A. Callaghan, C.W. Moeller, R. Ward, Inorg. Chem. 5 (1966) 1572–1576.
[4] J.M. Longo, P.M. Raccah, J.B. Goodenough, J. Appl. Phys. 39 (1968) 1327–1328.
[5] J.T. Rijssenbeek, R. Jin, Y. Zadorozhny, Y. Liu, B. Batlogg, R.J. Cava, Phys. Rev. B 59 (1999) 4561–4564.
[6] Y.S. Lee, J.S. Lee, K.W. Kim, T.W. Noh, J. Yu, E.J. Choi, G. Cao, J.E. Crow, Europhys. Lett. 55 (2001) 280–286.
[7] M. Drillon, L. Padel, J.-C. Bernier, J. Chem. Soc. Faraday Trans. II 75 (1979) 1193–1198.
[8] J.G. Zhao, L.X. Yang, Y. Yu, F.Y. Li, R.C. Yu, Z. Fang, L.C. Chen, C.Q. Jin, J. Solid State Chem. 180 (2007) 2816–2823.
[9] R.D. Burbank, H.T. Evans Jr., Acta Crystallogr. 1 (1948) 330–336.
[10] E. Quarez, M. Huvé, F. Abraham, O. Mentré, Solid State Sci. 5 (2003) 951–963.
[11] P. Lightfoot, P.D. Battle, J. Solid State Chem. 89 (1990) 174–783.
[12] J.T. Rijssenbeek, P. Matl, B. Batlogg, N.P. Ong, R.J. Cava, Phys. Rev. B 58 (1998) 10315–10318.
[13] Y. Doi, K. Matsuhira, Y. Hinatsu, J. Solid State Chem. 165 (2002) 317–323.
[14] P.C. Donohue, L. Katz, R. Ward, Inorg. Chem. 5 (1966) 339–342.
[15] H.-U. Schaller, A. Ehmann, S. Kemmler-Sack, Mater. Res. Bull. 19 (1984) 517–523.
[16] T. Negas, R.S. Roth, J. Solid State Chem. 3 (1971) 323–339.
[17] E.J. Cussen, P.D. Battle, Chem. Mater. 12 (2000) 831–838.
[18] Y. Syono, S.-I. Akimoto, K. Kohn, J. Phys. Soc. Jpn. 26 (1969) 993–999.
[19] T. Sugiyama, N. Tsuda, J. Phy. Soc. Jpn. 68 (1999) 1306–1312.
[20] G. Cao, S. Chikara, X.N. Lin, E. Elhami, V. Durairaj, P. Schlottmann, Phys. Rev. B 71 (2005) 035101.
[21] R.A. Young, The Rietveld Method, IUCr/Oxford University Press, Oxford, 1995.
[22] R.D. Shannon, Acta Crystallogr. A 32 (1976) 751–767.
[23] V. Markovich, I. Fita, R. Puzniak, E. Rozenberg, C. Martin, A. Wisniewski, A. Maignan, B. Raveau, Y. Yuzhelevskii, G. Gorodetsky, Phys. Rev. B 70 (2004) 024403.
[24] A.I. Shames, E. Rozenberg, C. Martin, A. Maignan, B. Raveau, G. Andr, G. Gorodetsky, Phys. Rev. B 70 (2004) 134433.
[25] S.S. Manoharan, R.K. Sahu, M.L. Rao, D. Elefant, C.M. Schneider, Europhys. Lett. 59 (2002) 451–457.
[26] B. Raveau, A. Maignan, C. Martin, R. Mahendiran, M. Hervieu, J. Solid State Chem. 151 (2000) 330–334.
[27] A.J. Williams, A. Gillies, J.P. Attfield, G. Heymann, H. Huppertz, M.J. Martinez-Lope, J.A. Alonso, Phys. Rev. B 73 (2006) 104409.
[28] A.I. Shames, E. Rozenberg, C. Martin, A. Maignan, B. Raveau, G. André, G. Gorodetsky, Phys. Rev. B 70 (2004) 134433.
[29] Z.S. Gönen, J. Gopalakrishnan, B.W. Eichhorn, R.L. Greene, Inorg. Chem. 40 (2001) 4996–5000.
[30] R.K. Sahu, M.L. Rao, S.S. Manoharan, K. Dörr, K.-H. Müller, Solid State Commun. 123 (2002) 217–222.
[31] Z.S. Gönen, J. Gopalakrishnan, B.W. Eichhorn, Solid State Sci. 4 (2002) 773–778.
[32] T. Horikubi, N. Kamegashira, Mater. Chem. Phys. 65 (2000) 316–319.
[33] R.K. Sahu, S.S. Manoharan, J. Appl. Phys. 91 (2002) 7517–7519.
[34] S.N. Kaul, A. Semwal, H.-E. Schaefer, Phys. Rev. B 62 (2000) 13892–13895.
[35] J.B. Goodenough, Magnetism and the Chemical Bond, Wiley, New York, London, 1963.
[36] M. Jansen, B. Klinkert, S. Elschner, Mater. Res. Bull. 25 (1990) 1415–1420.